

Research Article

Effects of Microstructure Variations on Macroscopic Terahertz Metafilm Properties

John F. O'Hara, Evgenya Smirnova, Abul K. Azad, Hou-Tong Chen, and Antoinette J. Taylor

Los Alamos National Laboratory, P.O. Box 1663, MS K771, Los Alamos, NM 87545, USA

Received 4 September 2007; Accepted 12 October 2007

Recommended by Yalin Lu

The properties of planar, single-layer metamaterials, or metafilms, are studied by varying the structural components of the splitting resonators used to comprise the overall medium. Measurements and simulations reveal how minor design variations in split-ring resonator structures can result in significant changes in the macroscopic properties of the metafilm. A transmission-line/circuit model is also used to clarify some of the behavior and design limitations of the metafilms. Though our results are illustrated in the terahertz frequency range, the work has broader implications, particularly with respect to filtering, modulation, and switching devices.

Copyright © 2007 John F. O'Hara et al. This is an open access article distributed under the Creative Commons Attribution License, which permits unrestricted use, distribution, and reproduction in any medium, provided the original work is properly cited.

1. INTRODUCTION

Following its initial theoretical [1, 2] and experimental [3] introductions, metamaterials research has experienced explosive growth and interest. Metamaterials are typically defined as artificial electromagnetic materials comprised of arrays of subwavelength ($\sim\lambda/10$) metallic resonators within or on a dielectric or semiconducting substrate. Due to the small dimensions of the resonators, these composites can be considered effective media [4], and can be quantitatively described by bulk constitutive parameters $\mu(\omega)$, and $\epsilon(\omega)$, in accordance with the macroscopic form of Maxwell's equations [5, 6]. More recently, the concept of the planar metamaterial, also known as a metafilm or metasurface, has taken on a clearer meaning. A metafilm, as the name implies, is simply a single, planar layer of metamaterial resonator elements [7]. Metafilms can be thought of as the bridge between three-dimensional (3D) metamaterials and the so-called frequency-selective surfaces [8]. The functionality of frequency-selective surfaces is based on the periodicity of the constituent elements, and is described by coherent wave interference concepts such as Bloch waves or Floquet modes [8–10]. Conversely, metafilms function on the same basis as metamaterials; their macroscopic properties depend mostly on the structure of the subwavelength resonators, and not necessarily on their periodic distribution.

While metamaterials promise novel devices and interesting science over very broad frequency bands, the terahertz (THz) spectrum (0.1–4 THz, $\lambda = 75\ \mu\text{m}$ –3 mm) represents a particularly interesting region. Electronic component technology is only just beginning to develop in the THz and remains extremely immature. Optical approaches to bridge the “THz gap” have met similar difficulty. The cause of this deficiency is a vivid lack of suitable materials from which to form the basic elements crucial to THz technology implementation on a large scale. Despite the numerous possible applications [11–14], presently high-power THz sources, efficient detectors, switches, modulators, filters, and other basic elements are not widely available. Metamaterials are optimistic candidates to correct this problem [15–20]. Additionally, the THz regime also serves as a scale model to investigate the dynamic nature and limitations of higher-frequency metamaterial designs. Continuing THz metamaterials research will become particularly relevant as new fabrication techniques and nanotechnology solutions continue to enable ever smaller resonator structures.

In this paper, we empirically study the microscale structural variations in split-ring resonators and their resulting impact on the macroscale effective properties of metafilms. In addition, we show how lumped-element circuit models can be used in conjunction with transmission-line theory to form an intuitive (though preliminary) analysis tool that could prove useful for designing specific metafilm properties.

TABLE 1: Unit cell dimensions.

Sample	All dimensions in μm				
	A_X	A_Y	L_X	L_Y	w
MF1	48	14	60	21	6
MF2	14	48	21	60	6
MF3	26	26	36	36	6
MF4	26	26	36	36	8
MF5	26	26	36	36	8
MF6	26	26	36	36	8
MF7	26	26	36	36	8

Most of the results shown are based on the simulated behavior of metafilms in THz transmission and reflection. However, we also show experimental transmission results to support the validity of the simulations.

2. EXPERIMENT AND SIMULATION

All of the metafilms studied in this work are based on the electric-resonator design [19–22] in which the symmetry of the split-ring resonator is used to eliminate or minimize the magnetic response. While the tuning of both the magnetic and electric metamaterial responses is sometimes desirable, certain applications, such as filtering, can also benefit from these new metamaterials that exhibit a purely electrical response. Our samples were comprised of planar, periodic arrays of electrical split-ring resonators (eSRRs) fabricated on semi-insulating gallium arsenide (SI-GaAs). The sample unit cells are illustrated in Figure 1 and detailed structural dimensions are given in Table 1. We add that the sample linewidths, $d = 2\ \mu\text{m}$, and gap spacing, $g = 2\ \mu\text{m}$, are equivalent for all samples. Sample fabrication utilized conventional photolithographic techniques in which the metal eSRRs, consisting of 200 nm of gold following 10 nm of titanium, were deposited on the SI-GaAs substrate of $625\ \mu\text{m}$ thickness. In total there were seven different metafilm designs, designated by the “MF” numbers shown in the figure.

Experimental characterization was performed with terahertz time-domain spectroscopy [23] (THz-TDS) operating in a confocal transmission geometry. A detailed description of this system can be found in [20, 24]. The linearly polarized THz beam was focused to a spot approximately 3 mm ($1/e$) in diameter and propagated normally through the samples. The total sample area of the metafilm was $(1 \times 1)\ \text{cm}^2$ to prevent beam clipping. Measurements were conducted in a dry-air environment to mitigate the effects of water vapor absorption. Transmission measurements were performed on the metafilm samples and, for reference, a bare SI-GaAs substrate of the same thickness. Since the THz measurement is coherent, we directly record the time-varying electric field of the transmitted THz radiation following passage through the sample. Numerical Fourier transformation of the measured time-domain data then permits the extraction of the frequency dependent complex transmission coefficient, $\tilde{t}(\omega) = t(\omega)e^{-j\phi(\omega)}$.

Figures 2 and 3 show the normalized frequency-dependent transmission coefficients, $t_{\text{Meas}}(\omega)$, obtained from our

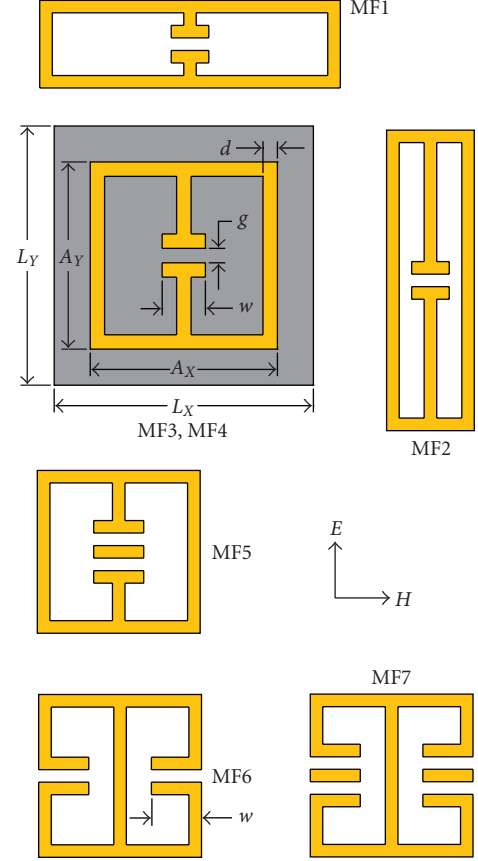


FIGURE 1: Metafilm unit cells. The dimensions L_X and L_Y specify the X and Y lattice parameters of the rectangular array on which the unit cells are distributed. Gold color indicates metallized regions whereas gray color indicates bare SI-GaAs regions. The THz field polarization is specified by the arrows to the right of MF5. All drawings are shown to scale except for the unit cell representing MF3 and MF4. To clarify dimensioning, this cell was magnified by 15%.

measurements. This data is normalized by dividing the measured transmission spectra of the metafilms, $E_{\text{MF}}(\omega)$, by the measured transmission spectrum of the reference substrate, $E_R(\omega)$, such that $t_{\text{Meas}}(\omega) = |\tilde{t}_{\text{Meas}}(\omega)| = |E_{\text{MF}}(\omega)/E_R(\omega)|$. All of the samples clearly exhibit a strongly resonant behavior between 0.5 and 1.1 THz in response to the electromagnetic field.

To further our understanding of the data, we performed simulations of the electromagnetic response of the metamaterials using commercially available finite-element software [25]; the results are shown in Figures 2 and 3. While simulations were set up to mimic the experimental conditions, some adjustments are necessary to properly compare the two.

These adjustments begin by recognizing that, in simulation, the substrate has an effectively infinite thickness to avoid Fabry-Perot (multiple reflection) effects in the frequency domain analysis. Therefore, simulated transmission coefficients are obtained by measuring the transmitted electric fields directly inside the GaAs, an obvious impossibility in our measurements. Instead our measured data must be divided by (or normalized to) a reference spectrum. This

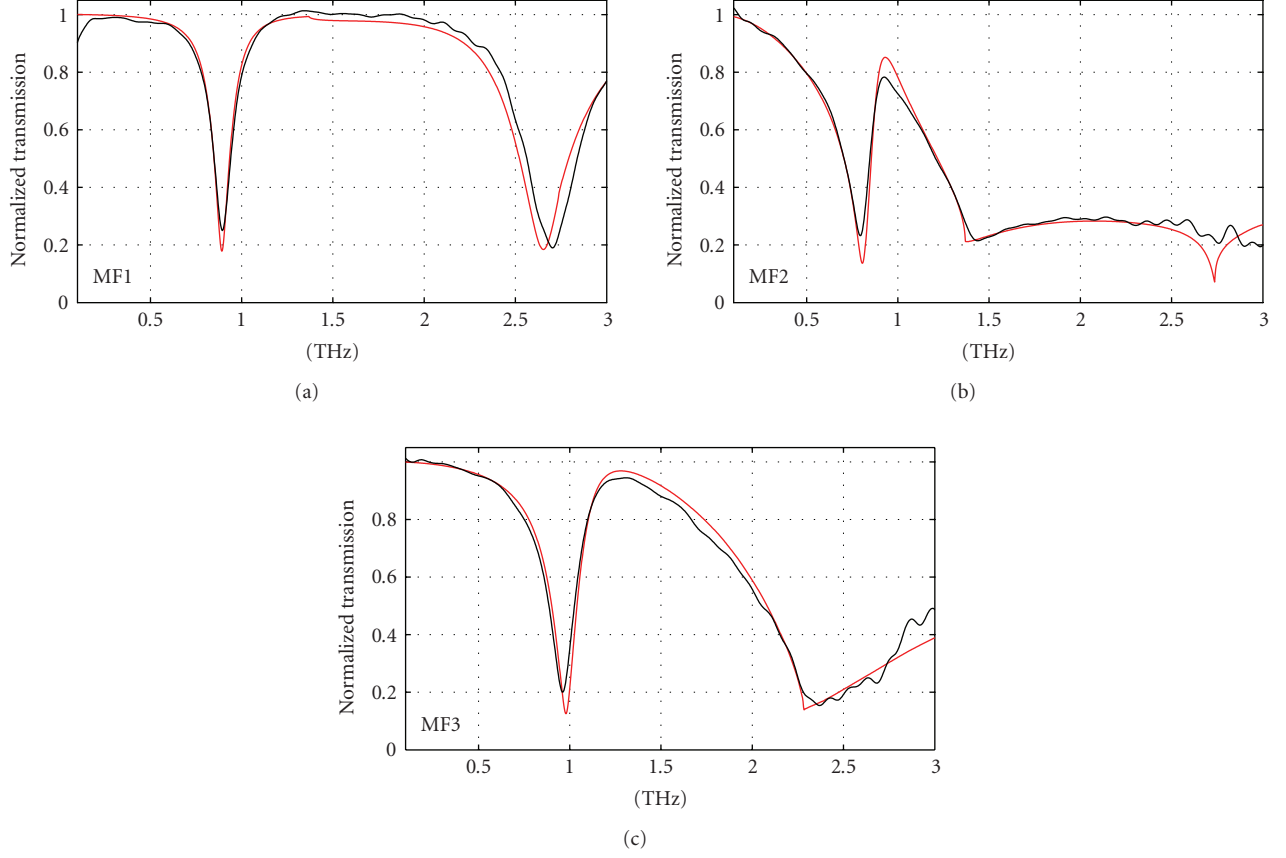


FIGURE 2: Normalized transmission through metafilm samples MF1, MF2, and MF3. Black curves indicate measured data while red curves show simulation results.

process isolates the response of the metafilm from the substrate by removing their common effects, such as Fresnel reflections from the back face. We add that Fabry-Perot effects can also be ignored in our measured data because our time-domain system allows us to “gate out” later arriving pulses. To quantify this data extraction procedure, we write out the expressions for the transmitted fields as a function of the input field, E_0 . For the bare reference substrate, the measured field, E_R , is determined by the transmission coefficients at the front and back faces:

$$E_R(\omega) = E_0 \frac{2Z_G}{Z_G + Z_0} \frac{2Z_0}{Z_G + Z_0}, \quad (1)$$

where $Z_G = 103 \Omega$ is the impedance of the GaAs substrate and $Z_0 = 377 \Omega$ is the impedance of free space. We have omitted the phase term associated with wave propagation through the substrate as this is common to the sample and reference measurements. For the metafilm samples, the transmitted electric field is equivalent, with the exception that Z_G is replaced by the complex metafilm impedance $Z(\omega)$ at the front face of the GaAs:

$$E_{MF}(\omega) = E_0 \frac{2Z(\omega)}{Z(\omega) + Z_0} \frac{2Z_0}{Z_G + Z_0}. \quad (2)$$

The ratio of these two expressions, \tilde{t}_{Meas} , describes what we actually measure. The magnitude of this quantity, t_{Meas} , is shown by the black curves in Figures 2 and 3:

$$t_{\text{Meas}}(\omega) = |\tilde{t}_{\text{Meas}}(\omega)| = \left| \frac{2Z(\omega)}{Z(\omega) + Z_0} \frac{Z_G + Z_0}{2Z_G} \right|. \quad (3)$$

Unlike our measurements, the simulations require no accounting for Fresnel reflections at the back substrate face and phase accumulations due to wave propagation in the substrate can be divided out. Therefore, the transmission coefficients are described by a much simpler equation

$$t_{\text{Sim}}(\omega) = |\tilde{t}_{\text{Sim}}(\omega)| = \left| \frac{2Z(\omega)}{Z(\omega) + Z_0} \right|. \quad (4)$$

We add that these transmission coefficients are equivalent to the complex S-parameter s_{21} , which is often the output returned by simulation software. From the equations, we see that to cast our simulations in the same form as the measured data we need only to multiply the simulations by $(Z_G + Z_0)/2Z_G = 2.33$. The results of this operation applied to our simulated transmission coefficients are shown as the red curves in Figures 2 and 3. The close agreement to measured data enables us to confidently use the simulated results in further studies. It also provides support for the experimental procedure of using a bare reference substrate to isolate the metafilm properties, despite the fact that

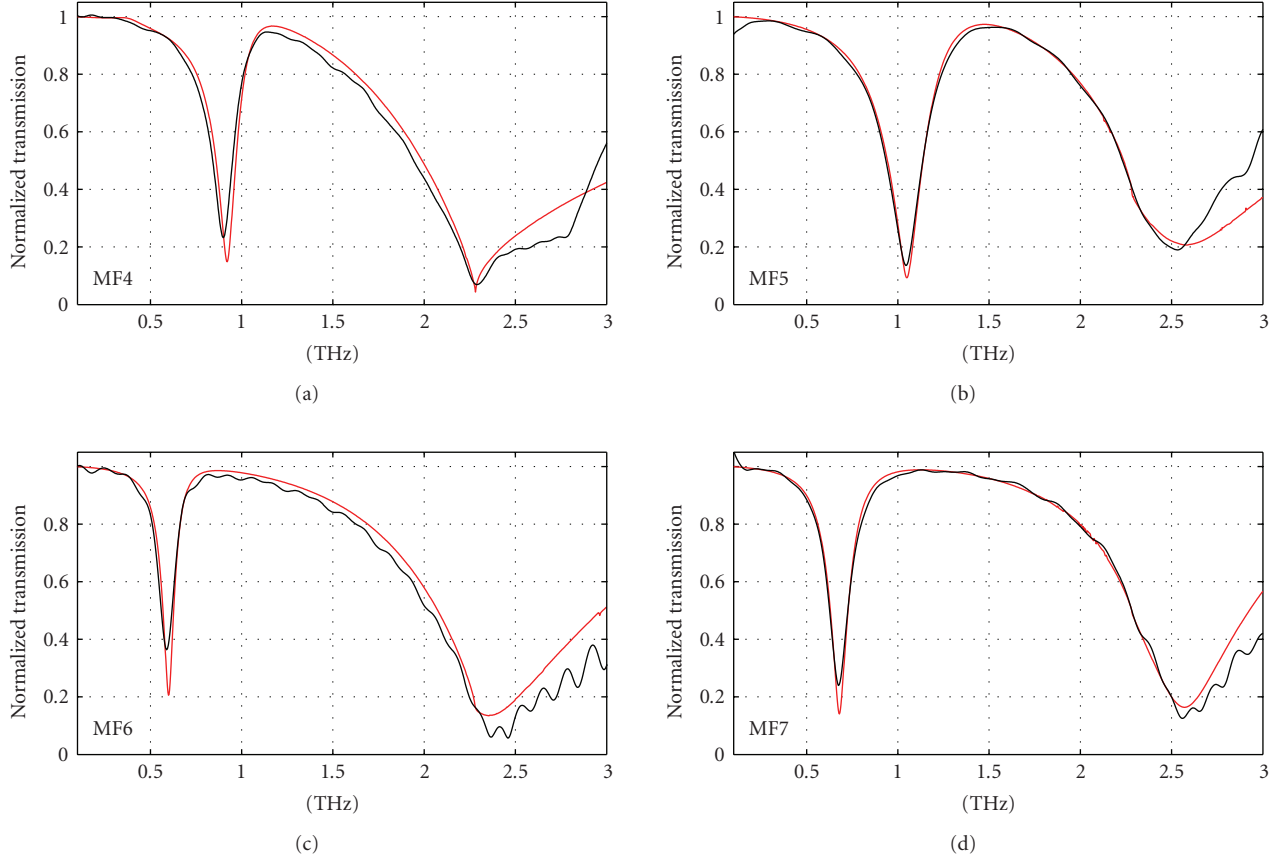


FIGURE 3: Normalized transmission through metafilm samples MF4, MF5, MF6, and MF7. Black curves indicate measured data while red curves show simulation results.

the metafilm’s properties are heavily influenced by the substrate. And finally, it foreshadows that the metafilm can be well described as a *two-dimensional* composite. In this sense, the metafilm can be thought of as a boundary-confined, or extremely thin, phase shifter, instead of a three-dimensional effective medium.

It is important to point out that the metafilm impedance $Z(\omega)$ used in (1)–(4) incorporates the effect of the *backing* substrate, which in this case is GaAs. Therefore, $Z(\omega)$ has some functional dependence on Z_G . However, if a wave was incident upon the GaAs side of the boundary, then $Z(\omega)$ would become dependent on Z_0 instead of Z_G ; in this case, free space is the backing substrate. The functional dependence on the backing material will be made clearer in a following section.

One particularly useful feature of the simulations is that they easily provide extra information, such as the reflection coefficient, $\tilde{r}(\omega) = s_{11} = r(\omega)e^{-j\phi(\omega)}$. The simulated reflection and transmission coefficients are shown by the black curves in Figures 4 and 5. We add that these plots are not normalized to a substrate spectrum, as was the case in Figures 2 and 3. By studying the simulations we can begin to understand the behavior of the metafilms. For example, in every sample t tends to the value 0.57 and r tends to 0.43 as the frequency approaches zero. Similar behavior can be seen between the high and low frequency resonances of each sam-

ple, and even out to high frequencies in some samples. We also observe that some samples have two very distinct and clean resonances, while others have highly asymmetric and overlapping resonances.

3. METAFILM BEHAVIOR AND MODELING

Using the simulations we can now discuss the relationships between the macroscale properties of our samples and their microscale differences. This begins by first addressing the variability in the rings themselves. As can be seen in Figure 1, all of the rings are modifications of the original two structures MF4 and MF6. All of the rings were further designed to have the same ring area of $672 \mu\text{m}^2$. Samples MF3, MF4, and MF5 differ only in modifications to the eSRR gaps. It is typically assumed that these gaps define the “capacitive” part of the eSRR response while the loops define the “inductive” part. This concept is illustrated in Figure 6(a) where the sample unit cells are modeled as lumped-element *RLC* circuits. This model is useful mainly in that it describes the Lorentzian nature of the resonance. One can use this model to roughly predict how our microstructural eSRR changes will affect the macroscale responses of our samples.

The resonant frequency of an *RLC* circuit is inversely related to the square root of both the inductance and capacitance. With this in mind, one can intuitively predict metafilm

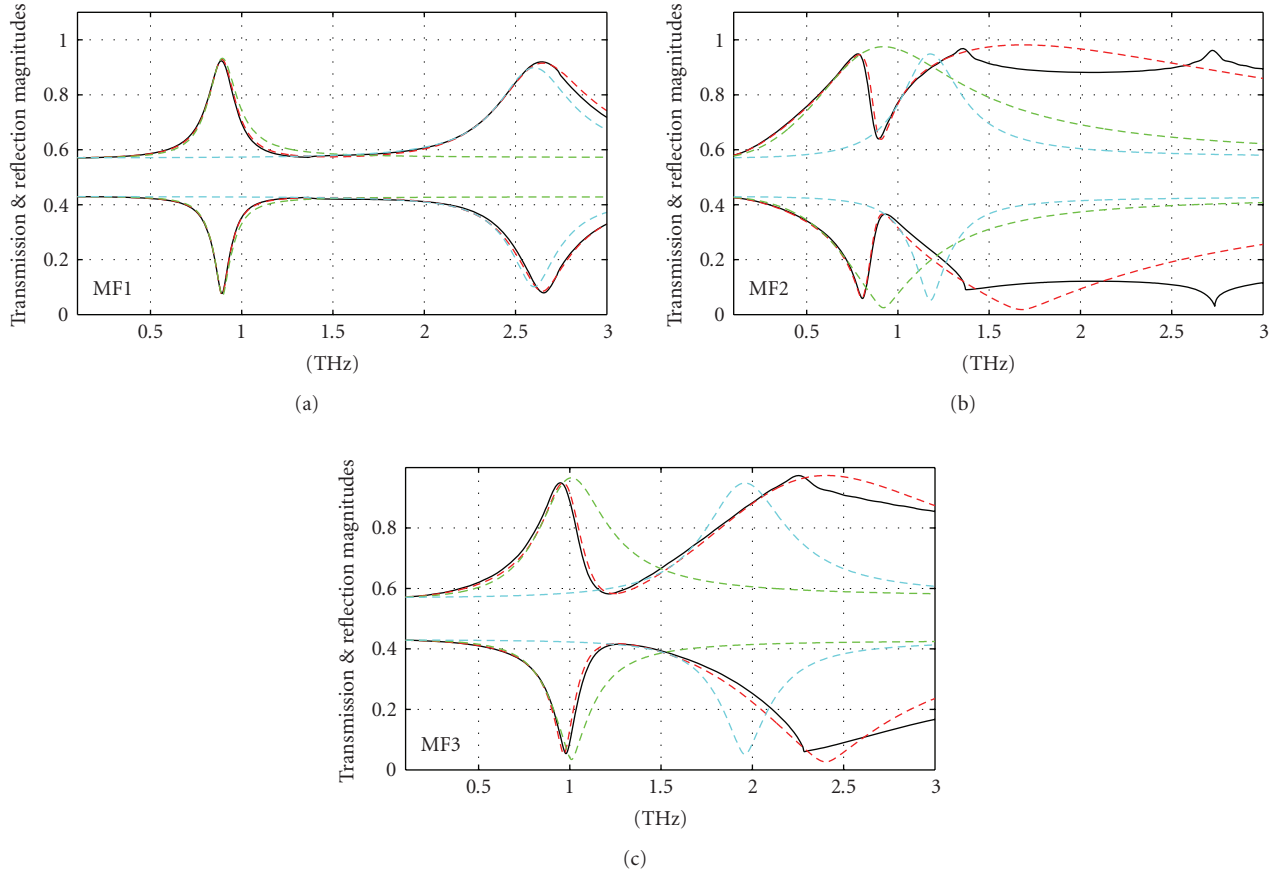


FIGURE 4: Transmission and reflection coefficients based on simulation and the TL-RLC circuit model for metafilm samples MF1, MF2, and MF3. Simulation results are shown in black. Red-dashed curves show the combined reflection and transmission coefficients based on the TL-RLC model. Green and blue dashed curves show the individual low and high frequency resonances, respectively, calculated by setting either R_1 or R_2 to a very large value.

behavior. For example, the extra metallic pad within the gap of MF5 can be regarded as splitting the capacitor into two coupled series capacitors, thus lowering the overall capacitance. The inductive response is largely determined by the area of the loops [2], so fixing the area and outer shape of the rings should, in principle, minimize the inductance as a performance variable. The net result is an increased resonance frequency. Indeed this is what we observe in Figure 5 by comparing MF4 and MF5. Similarly, MF6 should have roughly twice the capacitance (two capacitors in parallel) of MF4 causing a decrease in the resonance frequency; again this is consistent with the data. Sample MF7 is similar to MF6 where the added metallic pads decrease the capacitance with respect to MF6. The resonance frequency shifts up, as expected. Finally, by increasing the split gap width, w , sample MF4 should have a larger capacitance and slightly lower resonance frequency than MF3. Again this is observed in the data. We also point out an inverse relationship between capacitance and resonance linewidths in samples MF3–MF7. Those samples with the lower capacitance, or higher resonance frequency, also have broader linewidths.

Samples MF1 and MF2 are more radical variations; however, they maintain the same split gap and ring area as MF3

by stretching one dimension at the expense of shrinking another. One might expect that this alteration would have a minimal effect on the capacitance and, based on loop area, the inductance as well. In turn, we would expect little change in the lower frequency resonance. However, this is not the case. While the *position* of the lower frequency resonance does not shift greatly, the shape of this resonance is significantly altered. This is illustrated in Figure 4 by the green dashed curves which depict the first resonance after being mathematically separated from the higher-frequency resonance. This separation will be discussed in the following sections. One clear effect of changing the shape of the ring is to alter the linewidth of the lower resonance. An even greater effect observed in MF2 is the radical reshaping of the resonances. This behavior is due to a coupling effect occurring between the high and low frequency resonances. The high frequency resonance is usually understood to be due to dipole-dipole interactions between the two outside vertical (parallel to E-field) conductors of the rings. Since these conductors are relatively long on sample MF2, we expect this resonance to be shifted lower in frequency. The resulting close proximity between the low and high frequency resonances of this ring creates a strong coupling effect that reshapes the

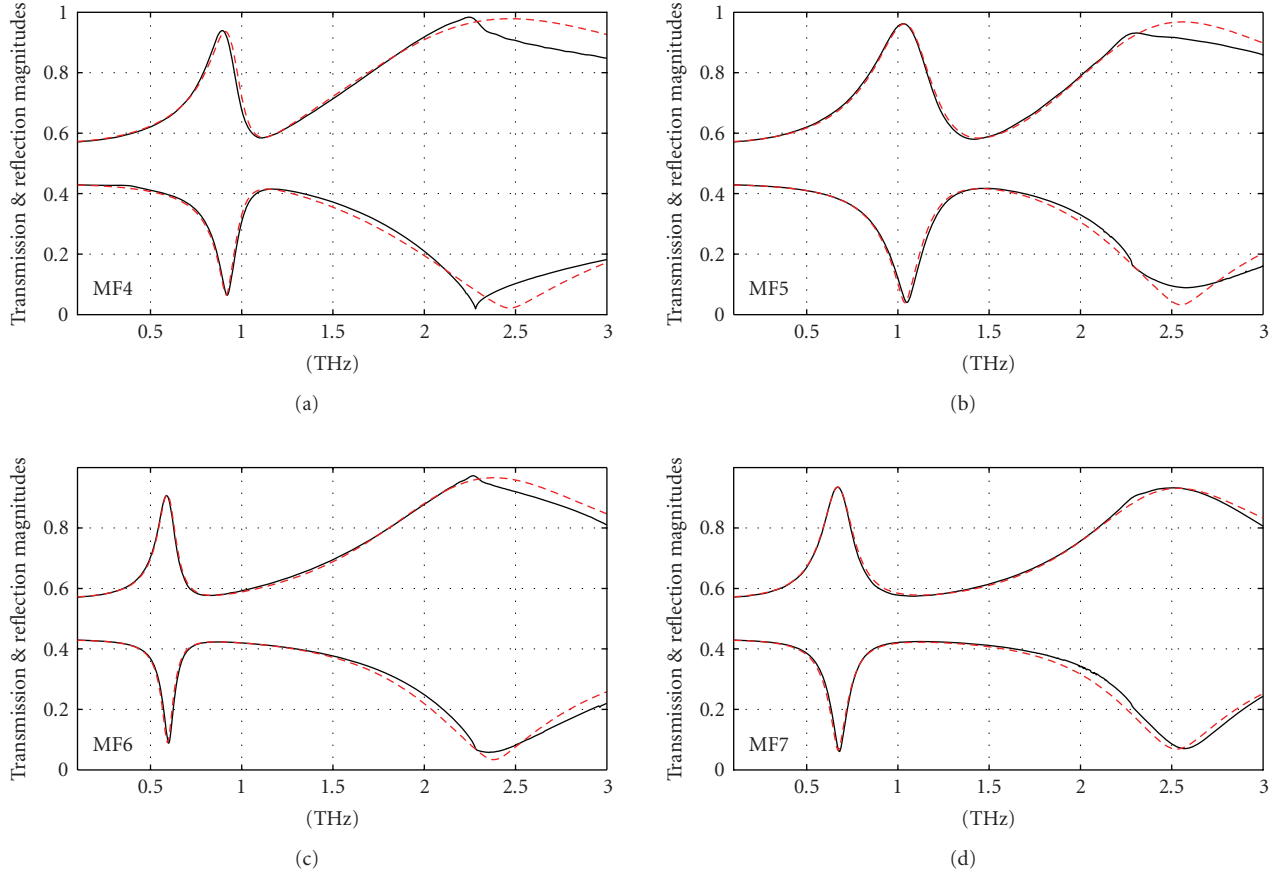


FIGURE 5: Transmission and reflection coefficients based on simulation and the TL-RLC circuit model for metafilm samples MF4, MF5, MF6, and MF7. Simulation results are shown in black. Red-dashed curves show the combined reflection and transmission coefficients based on the TL-RLC model.

transmission and reflection curves. The opposite is true for MF1, where the short vertical conductors shift the high frequency resonance to even higher values. Here the coupling effect is almost entirely eliminated and MF1 features very clean and distinct resonances.

We mention again that some samples have much narrower linewidths, or higher Q 's, than others. This is clearly an important attribute for possible future metamaterial devices. In filtering, for example, a narrow linewidth might be desirable for reducing noise. Broadband metamaterial devices such as detectors might benefit from ring designs that increase linewidth.

To help understand the origin of the observed transmission and reflection behavior it is helpful to derive a simple theoretical model of the metafilms. While the ring model of Figure 6(a) is intuitively helpful, a better model would incorporate other effects as well. As alluded to earlier, one approach is to treat the metafilm as an effective medium having some predetermined thickness, and a resonant permittivity with a Lorentzian functional form. This approach is valid for three-dimensional metamaterials in which planar layers of rings are spaced at a distance roughly equivalent to the unit cell length. However, our metafilms are essentially very thin, *single* metallic layers fabricated on relatively thick sub-

strates. This makes the concept of effective media difficult to implement. The main problem is the assignment of the effective thickness. If this thickness is less than that of the substrate, then the effective medium treatment artificially creates a boundary between the metamaterial layer and the substrate. Upon deriving the transmission coefficient of this effective metamaterial layer, that boundary will create Fresnel reflections resulting in Fabry-Perot effects. These effects are not present in the actual measurements, nor in the full EM simulations.

Alternatively, one can perform more rigorous electromagnetic calculations assuming known or derived forms for the electric and magnetic polarizabilities [7, 26]. While these approaches can be powerful, accurate, and widely applicable to diverse situations, they are relatively difficult to implement and do not generally provide an immediate intuition into the processes at work and their relation to macroscale behavior.

These troubles can be avoided by using the model shown in Figure 6(b). The model is similar to previously reported models [27] and utilizes a doubly resonant lumped-element circuit at the boundary of two TEM transmission lines (TLs). The two TLs represent the air and substrate while the resonant circuit represents the metafilm layer at their boundary. Since the metafilm is very thin, the lumped-element

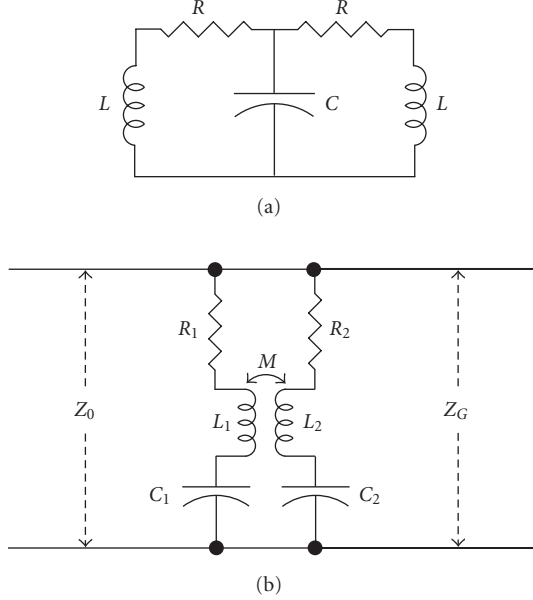


FIGURE 6: Circuit models for metafilm samples. (a) A series RLC circuit commonly used to describe the Lorentzian response of metamaterials. (b) The transmission-line RLC model which incorporates the effects of the substrate and uses a transformer to model the coupling between resonant modes.

approximation is valid in that the RLC circuit introduces no appreciable phase accumulation as the wave travels “through” it. Of course, the wave’s phase is affected by the circuit, but only in the sense of a boundary-induced phase shift. The metafilm, and its analogous TL- RLC model, can be quantitatively described with only a few equations. The transmission and reflection coefficients follow the normal form

$$\begin{aligned}\tilde{t}(\omega) &= \frac{2Z(\omega)}{Z(\omega) + Z_0}, \\ \tilde{r}(\omega) &= \frac{Z(\omega) - Z_0}{Z(\omega) + Z_0},\end{aligned}\quad (5)$$

where, like before, $Z_0 = 377 \Omega$ is the impedance of TL_0 and $Z(\omega)$ is the complex impedance of the metafilm. $Z(\omega)$ can be obtained by noting that the impedance at the metafilm boundary is the parallel combination of the RLC circuit impedance and the impedance of TL_G , which is $Z_G = 103 \Omega$. The impedance of the RLC circuit alone is

$$Z_{\text{ckt}}(\omega) = \frac{Z_{r1}Z_{r2} + \omega^2M^2}{Z_{r1} + Z_{r2} - j\omega 2M}, \quad (6)$$

where Z_{r1} and Z_{r2} are the impedances of the individual series circuits, $R_1L_1C_1$ and $R_2L_2C_2$, spanning the transmission line and M is the inductive coupling between these circuits. Both individual circuits have impedances of the form

$$Z_{rx} = R_x + j\omega L_x + \frac{1}{j\omega C_x}. \quad (7)$$

We clarify here that Z_{ckt} is not the impedance used in (1)–(4) because it does not include the effect of the backing substrate, which is integral to the metafilm behavior. Rather Z_{ckt} is only a conceptual 2D phase shifting and absorption layer, which can be combined with the backing substrate Z_G to obtain the effective metafilm impedance $Z(\omega)$. Again, this is accounted for by computing the parallel impedance of Z_{ckt} and Z_G . The result is

$$Z(\omega) = \frac{Z_G(Z_{r1}Z_{r2} + \omega^2M^2)}{Z_G(Z_{r1} + Z_{r2} - j\omega 2M) + Z_{r1}Z_{r2} + \omega^2M^2}. \quad (8)$$

A brief discussion of the limiting cases highlights some of the model’s behavior. For $M = 0$, there is no coupling between the low and high resonances of the metafilm. In this case, the metafilm response $Z(\omega)$ is the parallel combination of the two RLC resonances and the substrate. Based on (7), it is clear that at low frequencies ($\omega \rightarrow 0$), both $Z_{r1} \rightarrow \infty$ and $Z_{r2} \rightarrow \infty$. Hence the overall impedance presented to the incident wave is Z_G . This clarifies why the simulated transmission and reflection coefficients for every sample tend to 0.43 and 0.57, respectively; these values represent t and r for the bare substrate. Consequently, the metafilm is essentially transparent to the incoming wave at off-resonance frequencies, an important implication in filtering applications. For our model, similar behavior occurs at very high frequencies when $M = 0$. This is generally not observed in the actual sample measurements or simulations due to the higher-order resonances. For frequencies near the resonance of one or the other RLC circuit, the impedance drops sharply, causing a local maximum in r and a minimum in t . As the coupling parameter M departs from zero, the neighboring circuit affects the magnitude of this impedance drop. The coupling effect on the overall response is most drastic when the two RLC circuits have closely spaced resonances.

The task remains to match this model with the data. This is done by choosing the values of R_1 , L_1 , C_1 , R_2 , L_2 , C_2 , and M that result in t and r most closely overlapping the data. Limitations to these values are immediately obvious. For example, L ’s and C ’s must be paired to ensure that $\omega = 1/\sqrt{LC}$ is approximately equal to one or the other resonance frequency. Similarly, the resonance linewidths can be roughly matched by adjusting C and L simultaneously in an inverse relationship. Figures 4 and 5 show the comparison between the simulations (black curves) and the TL- RLC model (red-dashed curves). Table 2 shows the parameter values used to obtain these matches. The model clearly matches the simulated data well except at higher frequencies where higher-order modes become significant. The circuit parameters shown in Table 2 were obtained by manual adjustments and observation of the resulting match to simulations. The ease with which this is accomplished is dependent upon how clean the resonances are. Sample MF2, for example, has highly asymmetric resonances that complicate the determination of the “correct” RLC values. The nonintuitive nature of this match can be seen in Figure 4, where we show the individual resonances obtained by setting either R_1 or R_2 to a very large value. The positions of the individual resonances can be significantly shifted from their apparent positions in the transmission and reflection coefficients.

TABLE 2: Circuit parameters for matching TL-RLC model to simulated data. Resistor values are given in Ohms, capacitor values in femtofarads, and inductor values and coupling coefficients in picohenries.

Structure	Circuit component						
	R_1 (Ω)	L_1 (pH)	C_1 (fF)	R_2 (Ω)	L_2 (pH)	C_2 (fF)	M (pH)
MF1	15	90.0	0.352	25	38.0	0.099	-10.0
MF2	5	15.3	1.95	11	41.5	0.440	-15.0
MF3	7	31.0	0.790	11	33.0	0.210	-19.0
MF4	8	36.0	0.750	8	24.5	0.300	-18.0
MF5	6	29.0	0.770	13	25.0	0.200	-11.5
MF6	19	130	0.550	8	12.0	0.400	-10.0
MF7	13	74.0	0.750	20	18.0	0.240	-10.0

4. DISCUSSION

It is now necessary to discuss the extracted circuit parameters. We immediately point out that the circuit parameters in Table 2 do *not* necessarily correspond to the actual capacitance of the eSRR gap, the inductance of the eSRR loops, or the resistance of the conductors. In fact, the extracted values usually have the opposite behavior of what was expected. Taking the low frequency resonances as an example, we expect that the increased width of the split gap in MF4 would result in a larger capacitance than MF3. Surprisingly, the extracted capacitance, C_1 , of MF4 is lower than that of MF3 and the greatest change is observed in the inductance, L_1 . Another example is seen in the comparison of samples MF4 and MF5. The attempt here was to decrease the capacitance of the gap by inserting an intergap conductor. Instead, this variation hardly affected the capacitance of the model at all. Again, the inductive response was most affected. Indeed the parameters of Table 2 appear to have a “dual” characteristic in comparison to expectations. Where we expect large changes in capacitance, we observe large changes in inductance and vice versa.

The cause of this contrary behavior is that our model tells us little about real eSRR microparameters such as gap capacitance. The model only mimics the functional behavior of the metafilm by means of resonant circuits. The same behavior could be generated with two coupled systems comprised of springs, masses, and dashpots, although this would clearly have no relation whatsoever to a split-ring resonator. It is possible, however, that a model based on the dual circuit to that of Figure 6(b) may provide a better intuitive description of the relationship between macroscale performance and microscale variations. The exact form of this dual model is currently being studied and may constitute a closer match to previous circuit models [27]. Regardless, the value of the model is that it provides some metafilm analysis tools and also defines certain functional boundaries. For example, samples MF1, MF2, and MF3 all share a ring area of $672 \mu\text{m}$, but both the inductive, L_1 , and capacitive, C_1 response varied by almost as much as 6 times. While we cannot ensure true eSRR inductance or capacitance values we can say that neither of these quantities remains constant as the ring shape

is changed. This is important because simultaneous and inverse adjustments in L and C are exactly the method used to tune resonator linewidths while preventing resonance shifts.

The model provides another interesting insight into linewidth limitations. The metafilm is bounded on its sides by both air and GaAs, both of which affect the macroscale properties of the metafilm, at least in part, by altering the capacitance of the split-gap. But the model also shows that they limit how narrow a linewidth can be achieved for a metafilm filter of the kind shown in this work. Consider the case where $R = 0$ in the circuit of Figure 6(a). For this undamped circuit, the result of removing any resistance is an infinitely narrow resonance. However, in the TL-RLC model, the metafilm impedance is intimately linked with the bounding substrate impedance, so there can never be an “undamped” situation, even when $R_1 = 0$. The backing substrate always provides a finite impedance by which to prevent infinitely narrow metafilm linewidths. However, it is also clear that by choosing a substrate with a favorable impedance and properly tuning the eSRR inductance and capacitance, limited linewidth adjustment is possible.

The model also clarifies underlying behavior inherent in coupled-resonator systems. As previously shown, the model can be used to extract the *individual* behavior of the two coupled metafilm resonances. This is done by first adjusting model parameters to match the measured or simulated transmission or reflection coefficients. Then one of the resistance values, R_1 or R_2 , is assigned a very high value such that it behaves as an open circuit. This turns off one resonance and reveals the structure of the other. These individual resonances are displayed in Figure 4. Similarly, the model parameter M can be set to zero to observe the behavior of both resonances operating simultaneously but without coupling. Such tools are both intuitive and useful for a metafilm designer trying to achieve some desired behavior.

5. CONCLUSION

The potential uses of electric metafilms are numerous. For example, metafilms fabricated in the “complementary” fashion exhibit bandpass behavior in transmission yet retain a continuous and relatively thick metal layer over the substrate surface. These metafilms may serve as future grids or electrodes for biasing electronic components where a transparency window is desired. Existing “transparent” electrodes require extremely thin ~ 10 nm metallization to be both conducting and transparent. Metafilms offer obvious advantages in these cases, especially when high current densities are required. Further, dynamical control of metafilm properties is an important capability in the THz regime. This versatility offers tremendous possibilities for THz switches, modulators, and phase shifters.

We finally reiterate the advantage of studying microstructural variations in metamaterials. Our sample MF1 clearly shows a very clean resonant response in comparison to more traditional ring designs. This design offers a clear advantage for practical applications such as filtering. Moreover, with the continuing progression of more advanced metamaterials systems, such as negative-index materials, there is an obvious

need for reducing the complexity of the design procedure. The short ring, MF1, offers a vivid demonstration of decoupling two physical effects; such designs will become increasingly important in future metamaterial technology.

In conclusion, we have studied the behavior of a variety of new THz metamaterial designs through experimental THz time-domain transmission measurements and full electromagnetic simulations. The macroscale properties of these materials are seen to exhibit a strong dependence on microstructural variations, and are generally consistent with intuitive expectations. Using these results we were able to use a simple transmission-line and lumped-element circuit model that provides insight into the limitations and design tradeoffs for metamaterial performance. Though our work concentrated on the THz regime, it has wide applicability from the radio to the infrared spectra due to the scalability [28] of metamaterials, and metamaterials. The continued research of the fundamental properties of metamaterials will have a great impact on many future novel metamaterial-based devices.

ACKNOWLEDGMENTS

This work was performed, in part, at the Center for Integrated Nanotechnologies, a US Department of Energy, Office of Basic Energy Sciences, Nanoscale Science Research Center, operated jointly by Los Alamos and Sandia National Laboratories. Los Alamos National Laboratory, an affirmative action/equal opportunity employer, is operated by Los Alamos National Security, LLC, for the National Nuclear Security Administration of the US Department of Energy under Contract no. DE-AC52-06NA25396.

REFERENCES

- [1] V. G. Veselago, "The electrodynamics of substances with simultaneously negative values of ϵ and μ ," *Soviet Physics Uspekhi*, vol. 10, no. 4, pp. 509–514, 1968.
- [2] J. B. Pendry, A. J. Holden, D. J. Robbins, and W. J. Stewart, "Magnetism from conductors and enhanced nonlinear phenomena," *IEEE Transactions on Microwave Theory and Techniques*, vol. 47, no. 11, pp. 2075–2084, 1999.
- [3] D. R. Smith, W. J. Padilla, D. C. Vier, S. C. Nemat-Nasser, and S. Schultz, "Composite medium with simultaneously negative permeability and permittivity," *Physical Review Letters*, vol. 84, no. 18, pp. 4184–4187, 2000.
- [4] T. Koschny, M. Kafesaki, E. N. Economou, and C. M. Soukoulis, "Effective medium theory of left-handed materials," *Physical Review Letters*, vol. 93, no. 10, Article ID 107402, 4 pages, 2004.
- [5] Th. Koschny, P. Markoš, E. N. Economou, D. R. Smith, D. C. Vier, and C. M. Soukoulis, "Impact of inherent periodic structure on effective medium description of left-handed and related metamaterials," *Physical Review B*, vol. 71, no. 24, Article ID 245105, 22 pages, 2005.
- [6] For a review of the conditions of effective media applicable to metamaterials see ref. [5] and the references therein.
- [7] C. L. Holloway, M. A. Mohamed, E. F. Kuester, and A. Dienstfrey, "Reflection and transmission properties of a metamaterial with an application to a controllable surface composed of resonant particles," *IEEE Transactions on Electromagnetic Compatibility*, vol. 47, no. 4, pp. 853–865, 2005.
- [8] J. C. Vardaxoglou, *Frequency Selective Surfaces: Analysis and Design*, John Wiley & Sons, New York, NY, USA, 1997.
- [9] J. A. Kong, *Electromagnetic Wave Theory*, John Wiley & Sons, New York, NY, USA, 2nd edition, 1990.
- [10] H. Chen, L. Ran, D. Wang, J. Huangfu, Q. Jiang, and J. A. Kong, "Metamaterial with randomized patterns for negative refraction of electromagnetic waves," *Applied Physics Letters*, vol. 88, no. 3, Article ID 031908, 3 pages, 2006.
- [11] J. E. Davis, "Bandpass interference filters for very far infrared astronomy," *Infrared Physics*, vol. 20, no. 4, pp. 287–290, 1980.
- [12] D. A. Weitz, W. J. Skocpol, and M. Tinkham, "Capacitive-mesh output couplers for optically pumped far-infrared lasers," *Optics Letters*, vol. 3, no. 1, pp. 13–15, 1978.
- [13] F. Baumann, W. A. Bailey Jr., A. Naweid, W. D. Goodhue, and A. J. Gatesman, "Wet-etch optimization of free-standing terahertz frequency-selective structures," *Optics Letters*, vol. 28, no. 11, pp. 938–940, 2003.
- [14] R. D. Rawcliffe and C. M. Randall, "Metal mesh interference filters for the far infrared," *Applied Optics*, vol. 6, no. 8, p. 1353, 1967.
- [15] T. J. Yen, W. J. Padilla, N. Fang, et al., "Terahertz magnetic response from artificial materials," *Science*, vol. 303, no. 5663, pp. 1494–1496, 2004.
- [16] W. J. Padilla, A. J. Taylor, C. Highstrete, M. Lee, and R. D. Averitt, "Dynamical electric and magnetic metamaterial response at terahertz frequencies," *Physical Review Letters*, vol. 96, no. 10, Article ID 107401, 4 pages, 2006.
- [17] H.-T. Chen, W. J. Padilla, J. M. O. Zide, A. C. Gossard, A. J. Taylor, and R. D. Averitt, "Active terahertz metamaterial devices," *Nature*, vol. 444, no. 7119, pp. 597–600, 2006.
- [18] H.-T. Chen, W. J. Padilla, J. M. O. Zide, et al., "Ultrafast optical switching of terahertz metamaterials fabricated on ErAs/GaAs nanoisland superlattices," *Optics Letters*, vol. 32, no. 12, pp. 1620–1622, 2007.
- [19] H.-T. Chen, J. F. O'Hara, A. J. Taylor, et al., "Complementary planar terahertz metamaterials," *Optics Express*, vol. 15, no. 3, pp. 1084–1095, 2007.
- [20] J. F. O'Hara, E. Smirnova, H.-T. Chen, et al., "Properties of planar electric metamaterials for novel terahertz applications," *Journal of Nanoelectronics and Optoelectronics*, vol. 2, no. 1, pp. 90–95, 2007.
- [21] D. Schurig, J. J. Mock, and D. R. Smith, "Electric-field-coupled resonators for negative permittivity metamaterials," *Applied Physics Letters*, vol. 88, no. 4, Article ID 041109, 3 pages, 2006.
- [22] W. J. Padilla, M. T. Aronsson, C. Highstrete, M. Lee, A. J. Taylor, and R. D. Averitt, "Electrically resonant terahertz metamaterials: theoretical and experimental investigations," *Physical Review B*, vol. 75, no. 4, Article ID 041102, 4 pages, 2007.
- [23] D. Grischkowsky, S. Keiding, M. van Exter, and Ch. Fattinger, "Far-infrared time-domain spectroscopy with terahertz beams of dielectrics and semiconductors," *Journal of the Optical Society of America B*, vol. 7, no. 10, pp. 2006–2015, 1990.
- [24] J. F. O'Hara, J. M. O. Zide, A. C. Gossard, A. J. Taylor, and R. D. Averitt, "Enhanced terahertz detection via ErAs:GaAs nanoisland superlattices," *Applied Physics Letters*, vol. 88, no. 25, Article ID 251119, 3 pages, 2006.
- [25] "CST Microwave Studio ®, ©2005 CST—Computer Simulation Technology," Wellesley Hills, Mass, USA, December 2005, <http://www.cst.com>.
- [26] F. Falcone, T. Lopetegi, M. A. G. Laso, et al., "Babinet principle applied to the design of metasurfaces and metamaterials," *Physical Review Letters*, vol. 93, no. 19, Article ID 197401, 4 pages, 2004.

- [27] J. D. Baena, J. Bonache, F. Martín, et al., “Equivalent-circuit models for split-ring resonators and complementary split-ring resonators coupled to planar transmission lines,” *IEEE Transactions on Microwave Theory and Techniques*, vol. 53, no. 4, pp. 1451–1460, 2005.
- [28] W. J. Padilla, D. R. Smith, and D. N. Basov, “Spectroscopy of metamaterials from infrared to optical frequencies,” *Journal of the Optical Society of America B*, vol. 23, no. 3, pp. 404–414, 2006.



Hindawi

Submit your manuscripts at
<http://www.hindawi.com>

